scientific reports

Check for updates

OPEN

Targeting the VEGFR2 signaling pathway for angiogenesis and fibrosis regulation in neovascular age-related macular degeneration

Eunhye Yu[1], Haechan Kim[1], Hyeonji Park[2,3], Ji Hye Hong[2], Jonghwa Jin[2], Yunjeong Song[4], Je Moon Woo[5], Jung Kee Min[5]✉ & Jaesuk Yun[1]✉

Neovascular age-related macular degeneration (nAMD) is characterized by abnormal blood vessel growth from the choroid, leading to complications and eventual blindness. Despite anti-VEGF therapy, subretinal fibrosis remains a major concern, as VEGF/VEGF receptor-2 (VEGFR2) signaling can contribute to both angiogenesis and fibrosis. For the identification of the aqueous humor proteome, we performed liquid chromatography with tandem mass spectrometry analysis. To investigate the potential therapeutic effects of targeting the VEGF signaling pathway using apatinib, a highly selective VEGFR2 tyrosine kinase inhibitor, this study employed in vitro (THP-1 conditioned media-treated ARPE-19 cells) and in vivo (laser-induced choroidal neovascularization mouse) models of nAMD. This study revealed elevated VEGFR2 protein levels in the aqueous humor of nAMD patients, suggesting a potential target to mitigate neovascularization and fibrosis in nAMD. Apatinib effectively reduced VEGFA and αSMA levels in both in vitro and in vivo models. Moreover, apatinib showed improvement in laser-induced subretinal hyper-reflective lesions. The action mechanism was linked to the inhibition of VEGFR2 activation, leading to the suppression of both angiogenesis and fibrosis through the downregulation of STAT3 phosphorylation. Therefore, the VEGFR2 signaling pathway appears to play a central role in the development of nAMD by regulating both angiogenesis and fibrosis.

Keywords Apatinib, Choroidal neovascularization, Fibrosis, Neovascular age-related macular degeneration, Tyrosine kinase inhibitor, Vascular endothelial growth factor receptor-2

Neovascular age-related macular degeneration (nAMD) is characterized by the formation of abnormal blood vessels from the choroid and the growth of the new vessels into the space under the retinal pigment epithelium and/or the neurosensory retina. Such abnormal new vessels can easily cause blood, serous, and/or exudate fluid spillage, thereby decreasing central vision[1]. Vascular endothelial growth factor (VEGF), which promotes angiogenesis and increases vascular permeability, plays a key role in the intraocular neovascularization occurring in several pathological conditions[2]. Therefore, intravitreal anti-VEGF injection therapy could potentially reverse anatomical changes and improve vision in patients with nAMD[3–6]. However, approximately 45% of patients develop fibrotic scars 2 years after anti-VEGF treatment[7]. Various cell types, such as retinal pigment epithelial (RPE) cells, immune cells, and fibroblasts have been associated with this pathological process, which consequently creates scar tissue and causes blindness in patients with nAMD[1]. Therefore, preventing fibrosis after anti-VEGF monotherapy is an unmet medical need.

Endothelial cell function is regulated by the binding of VEGF to its receptors (VEGFR: VEGFR1, VEGR2, and VEGFR3). Among the three types of VEGF receptors, VEGFR2, which is mainly distributed in vascular

[1]College of Pharmacy, Chungbuk National University, 194-31, Osongsaengmyeong 1-ro, Osong-eup, Heungduk-gu, Cheongju-si, Chungcheongbuk-do 28160, Republic of Korea. [2]New Drug Development Center, Osong Medical Innovation Foundation, 123, Osongsaengmyeong-ro, Osong-eup, Heungduk-gu, Cheongju-si, Chungcheongbuk-do 28160, Republic of Korea. [3]College of Pharmacy, Chungbuk National University, 194-21, Osongsaengmyeong 1-ro, Osong-eup, Heungduk-gu, Cheongju-si, Chungcheongbuk-do 28160, Republic of Korea. [4]Ministry of Food and Drug Safety, 187, Osongsaengmyeong 2-ro, Osong-eup, Heungdeok-gu, Cheongju-si, Chungcheongbuk-do 28159, Republic of Korea. [5]Department of Ophthalmology, College of Medicine, Ulsan University Hospital, University of Ulsan, 25, Daehakbyeongwon-ro, Dong-gu, Ulsan 44033, Republic of Korea. ✉email: jkmin@uuh.ulsan.kr; jyun@chungbuk.ac.kr

endothelial cells, triggers the angiogenic action of VEGF. The VEGF family includes VEGFA, VEGFB, VEGFC, VEGFD, placental growth factor, VEGFE, and *Trimeresurus flavoviridis* svVEGF. Except for the latter two members, the rest of the genes in the VEGF family exist in the mammalian genome, including humans. Among these genes, VEGFA serves various functions, including promoting angiogenesis, regulating vascular permeability, and stimulating cell migration in the macrophage lineage and endothelial cells. Upon VEGFA binding, VEGFR2 is autophosphorylated at the cytoplasmic tyrosine residues, which promotes tyrosine phosphorylation of several signal transduction proteins. Thus, VEGFA/VEGFR2 binding triggers downstream signaling pathways of VEGF-induced endothelial cell proliferation, migration, and morphogenesis[8–10]. This signal can also directly regulate several profibrotic genes and significantly upregulate the expression of collagen and alpha smooth muscle actin (αSMA)[11,12]. VEGF is a well-known signal transducer and activator of transcription 3 (STAT3) target, indicating the key role of STAT3 in promoting angiogenesis and fibrosis[13–15]. Therefore, blocking STAT3 activity may attenuate both angiogenesis and fibrogenesis.

Apatinib (Rivoceranib, YN968D1, Selleck Chemicals, Houston, TX, USA; Fig. 1) is a potent and small-molecule tyrosine kinase inhibitor that selectively targets VEGFR2[16]. Given the importance of angiogenesis in

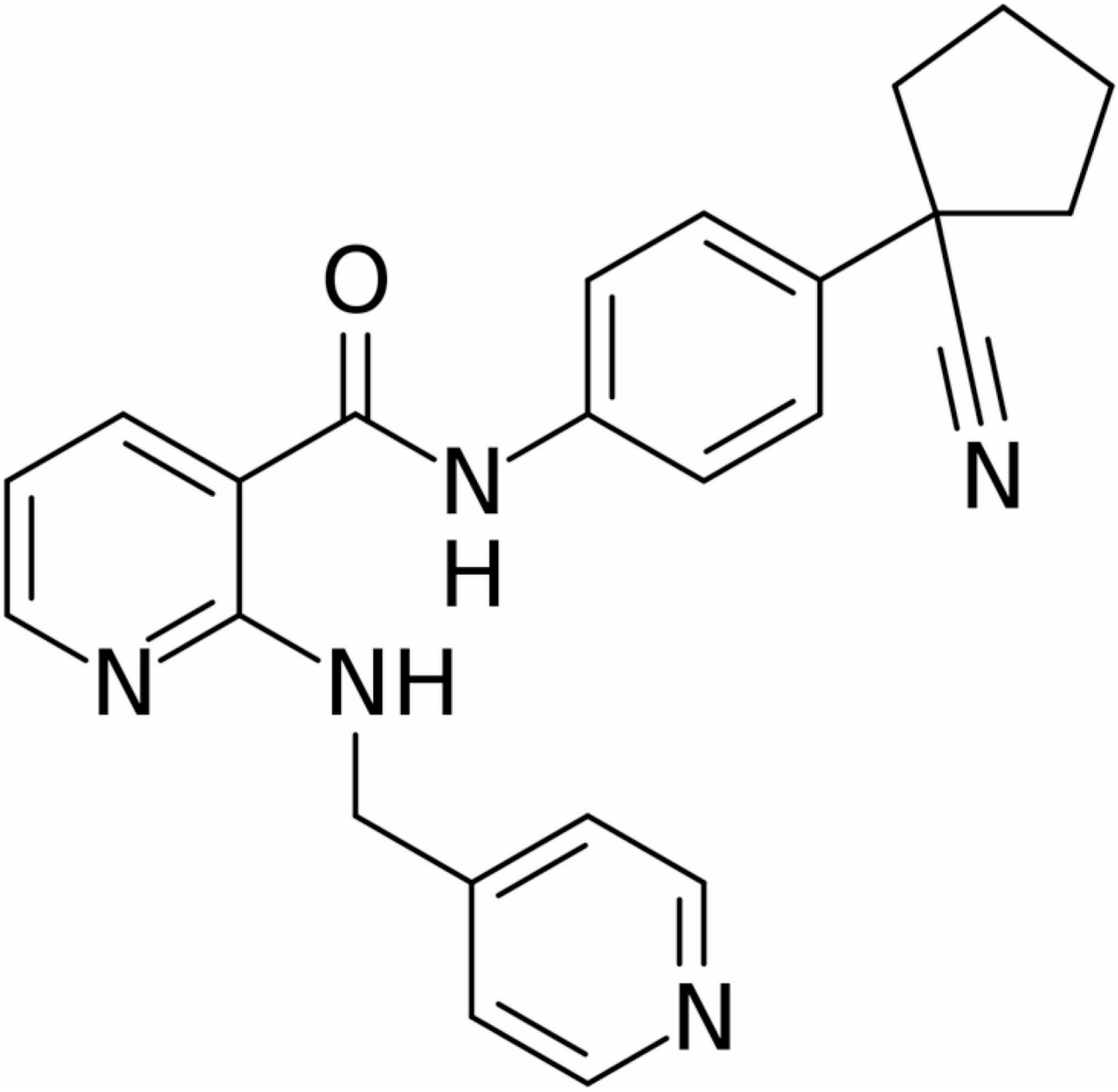

Fig. 1. Apatinib, a small-molecule receptor tyrosine kinase inhibitor, exhibits potential antiangiogenic and antineoplastic effects. It selectively binds to and inhibits vascular endothelial growth factor (VEGF) receptor 2, thereby potentially suppressing VEGF-stimulated endothelial cell migration and proliferation, consequently reducing neovascularization.

the development and progression of cancer, apatinib had initially been developed as an anticancer drug and is currently being studied as a third-line treatment option for advanced metastatic gastric cancer[17]. As a selective VEGFR2 tyrosine kinase inhibitor, apatinib can antagonize both VEGF and fibrotic signaling pathways by inhibiting VEGFR2 activation, which triggers downstream signaling that promotes endothelial cell proliferation, migration, and angiogenesis, and upregulates profibrotic genes such as αSMA and collagen through STAT3 activation[18–20]. Therefore, the current study explored whether apatinib exerts anti-choroidal neovascularization (CNV) and anti-fibrosis effects by selectively targeting VEGFR2 through in vitro and in vivo experiments.

Results

Identification of proteins in human aqueous humor

To comprehensively analyze the proteome of the aqueous humor, we employed the TMT labeling method in conjunction with LC-based mid pH peptide fractionation. High-resolution mass spectrometry was utilized for protein identification, and data were analyzed using multiple database search tools including SEQUEST and X!Tandem. Our analysis resulted in the identification of 627 protein groups meeting stringent criteria: each identified protein group had a minimum confidence level of > 95%, was supported by more than one unique peptide, and exhibited a false discovery rate (FDR) of less than 5%. Detailed information on the identified protein groups can be found in Supplementary Table S2.

Differential expression of proteins in the aqueous humor of nAMD and control groups

To distinguish the proteome profiles between patients with nAMD and control subjects, we performed three technical replicates and used TMT-labeled quantification to compare protein expression under various conditions. We applied rigorous criteria to identify key proteins with differential expression, including a t-test p-value below 0.05, a confidence level above 95%, a minimum of two unique peptides, and an FDR of less than 5%. Additionally, we used fold-change thresholds expressed as a log2 ratio greater than 1.5 or less than −1.5 to pinpoint significant differences in protein expression. A total of 127 proteins met these criteria (Supplementary Table S3), and differentially expressed proteins were depicted in volcano plots (Fig. 2). To understand the functions of these proteins in aqueous humor samples, we used Gene Ontology (GO) to classify them by biological process (BP), cellular component (CC), and molecular function (MF). Our analysis revealed significant enrichment of proteins involved in cell adhesion, acute-phase response, and response to hydrogen peroxide in aqueous humor samples. The GO analysis for molecular function (MF) revealed significant enrichment in categories such as extracellular matrix structural constituent, structural molecule activity, integrin binding, antioxidant activity, cell adhesion molecule binding, serine-type endopeptidase inhibitor activity, structural constituent of eye lens, fibronectin binding, growth factor activity, and calcium ion binding. Additionally, proteins associated with extracellular region, extracellular space, and extracellular exosome were significantly enriched according to GO analysis of cellular components (Supplementary Figure S1).

To analyze biological functions related to macular degeneration, we performed GO analysis using the DABID tools. As a result of GO analysis, proteins associated with angiogenesis and fibrosis were analyzed and compared between control and nAMD (Table 1). Seven proteins (ANPEP, APOA4, CCN3, ERAP1, FLT1, KDR, and PPBP) were involved in angiogenesis and were all upregulated. Nine proteins (CAT, CFD, COL1A1, DSP, FLT1, LGALS1, LGALS3BP, SERPINA1, and TIMP1) were involved in fibrosis and were all upregulated except for DSP and LGALS3BP. Furthermore, the quantitation of FLT1 (VEGFR1) and KDR (VEFGR2), which triggers the angiogenic action of VEGF, revealed higher expression in nAMD compared to control.

Apatinib reduced VEGFA, αSMA, and p-STAT3 expression induced by TCM in ARPE-19 cells

ARPE-19 cells were stimulated by TCM for 3 h in 96-well plates and then dose-dependently treated with apatinib or bevacizumab. After 3 h of treatment, the change in VEGFA and αSMA expression in ARPE-19 cells was evaluated. The TCM-induced increase in fluorescence intensity of VEGFA and αSMA was significantly decreased in ARPE-19 cells after co-treatment with apatinib (Fig. 3a–d). Also, STAT3 phosphorylation increased significantly but was significantly suppressed by apatinib (Fig. 3e, TCM group: $F(1,8) = 5.668$, $p = 0.044$; apatinib group: $F(1,8) = 3.325$, $p = 0.106$; interaction: $F(1,8) = 2.360$, $p = 0.163$).

Apatinib reduced the size of CNV in the laser-induced CNV mouse model

To assess apatinib's impact on CNV progression, we measured CNV size in mice after laser-induced CNV. Following laser photocoagulation, mice received either a single intravitreal injection or a single subconjunctival injection of apatinib. Intravitreal injection of bevacizumab was used as a positive control. After one week, CNV lesions were visualized by staining choroidal vasculature with isolectin B4. Accordingly, eyes treated with apatinib and bevacizumab had fewer CNV lesions than did eyes that did not receive the same treatment (Fig. 4).

Apatinib reduced the expression level of VEGFA and αSMA in mice with laser-induced CNV

Western blot assay was conducted to assess the impact of apatinib on the expression of VEGFA and αSMA in mice with laser-induced CNV. Seven days following laser photocoagulation, proteins were extracted from the eyeballs of experimental mice. The levels of VEGFA and αSMA were analyzed using Western blotting, with GAPDH serving as an internal loading control (Fig. 5a). Eyes treated with apatinib (both intravitreal and subconjunctival injections) had lower expression levels of VEGFA and αSMA than did eyes that received laser photocoagulation alone (Fig. 5b; $F(3,28) = 5.07$, $p = 0.006$; Fig. 5c; $F(3,28) = 15.902$, $p < 0.001$).

Similarly, the effect of bevacizumab administered via intravitreal injection was also assessed and found to produce similar reductions in the expression levels of VEGFA and αSMA. Detailed results of bevacizumab's effects are provided in the supplementary figure S2 (Figure S2. [VEGFA]; $F(2,17) = 9.507$, $p = 0.002$; [αSMA]; $F(2,17) = 9.814$, $p < 0.001$).

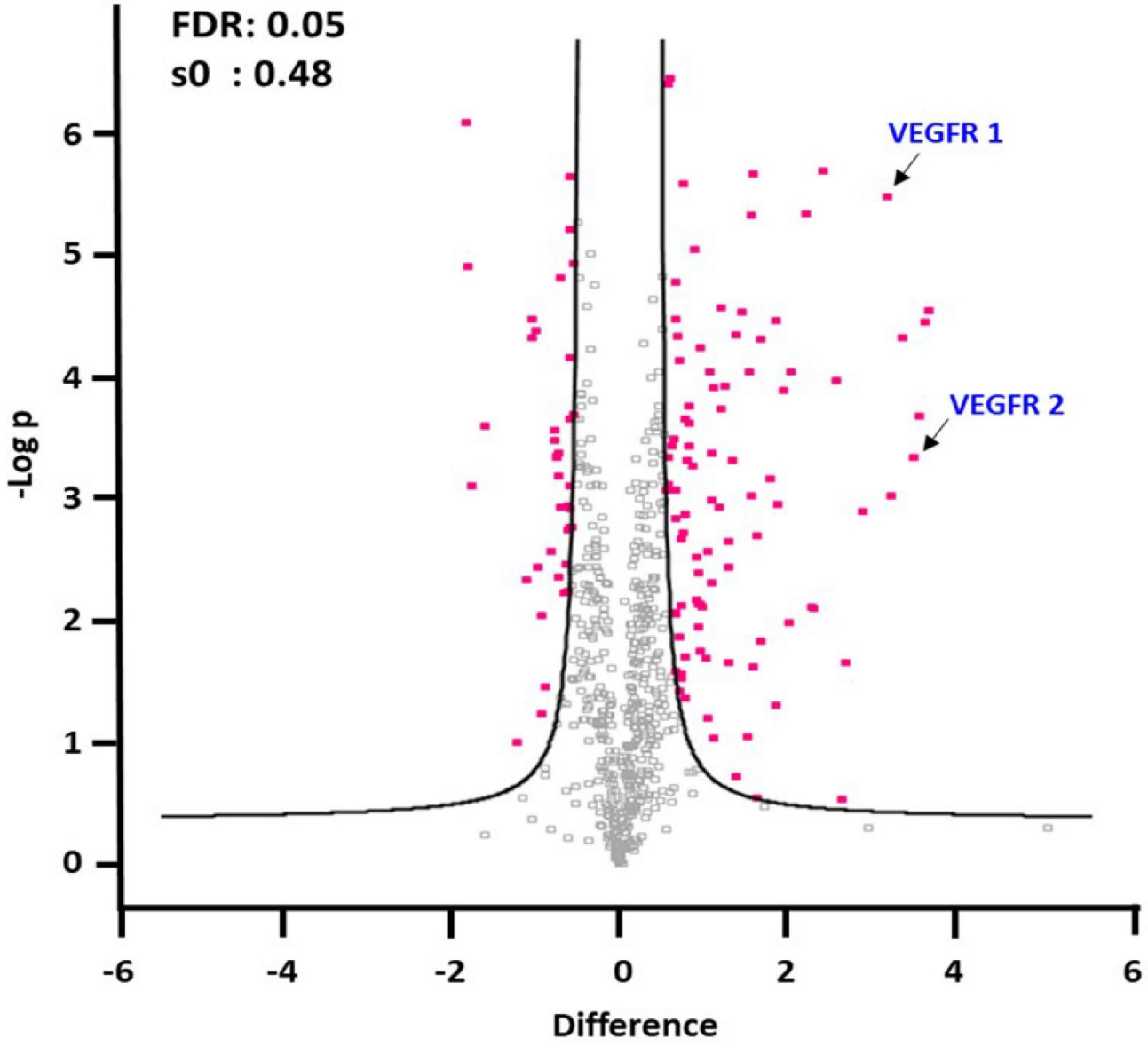

Fig. 2. Differentially expressed proteins in the aqueous humor of patients with nAMD and control group. Quantitation of VEGFR1 and VEFGR2, which trigger the angiogenic action of VEGF, showed that they significantly upregulated in nAMD compared to control. The cutoff criteria for protein quantitation were as follows: t-test, $p < 0.05$, minimum confidence level > 95%, more than two unique peptides, FDR < 5%, and fold-change thresholds (expressed as log2 ratio) of > 1.5 or < − 1.5. For the analysis of differentially expressed proteins and statistical analysis, Perseus (version 1.5.8.2) was used, where the cutoff criteria for significant fold change (FC) and t-test p values were set at ± 1.5 and 0.05, respectively.

Morphological changes induced by laser photocoagulation

For examination of morphological changes in mice eyes following laser-induced photocoagulation, mice were euthanized through quick cervical dislocation 7 days post laser treatment, intended for subsequent immunohistochemical analysis. In horizontal sections of the eyes, subretinal infiltrates and fibrosis were observed in laser-exposed subretinal lesions. αSMA expression was observed 7 days after laser photocoagulation (Fig. 6).

Apatinib attenuated hyper-reflective lesions in mouse retina with the laser-induced CNV

A hyper-reflective lesion is a morphological feature observed on OCT as hyper-reflective material located inside and/or outside the retina, and internal to the retinal pigment epithelium. This lesion has several elements, including fluid, fibrin, blood, scar, and/or fibrovascular tissue[21]. The increase in hyper-reflective lesions were confirmed on OCT of mice with laser-induced CNV. This hyper-reflective lesion area decreased significantly after intravitreal administration of apatinib (1 μg/1 μL in DMSO) and bevacizumab as positive control (25 μg/1 μL) (Fig. 7).

	Protein	Gene	nAMD/control (Log2 ratio)	p value	Gene ontology analysis
1	Adipsin	CFD	0.787	0.000	Fibrosis
2	Alpha-1-antitrypsin	SERPINA1	0.590	0.000	Pulmonary fibrosis
3	Aminopeptidase N	ANPEP	0.613	0.026	Angiogenesis
4	Apolipoprotein A-IV	APOA4	1.577	0.000	Angiogenesis
5	Catalase	CAT	1.557	0.000	Fibrosis
6	CCN family member 3	CCN3	0.980	0.019	Angiogenesis
7	Collagen alpha-1(I) chain	COL1A1	0.740	0.005	Pulmonary fibrosis
8	Desmoplakin	DSP	−0.600	0.002	Fibrosis
9	Endoplasmic reticulum aminopeptidase 1	ERAP1	1.047	0.014	Angiogenesis
10	Galectin-1	LGALS1	1.353	0.001	Pulmonary fibrosis
11	Galectin-3-binding protein	LGALS3BP	−0.593	0.000	Pulmonary fibrosis
12	Metalloproteinase inhibitor 1	TIMP1	0.680	0.001	Fibrosis
13	Platelet basic protein	PPBP	1.300	0.003	Angiogenesis
14	Vascular endothelial growth factor receptor 1	FLT1	3.213	0.000	Angiogenesis, pulmonary fibrosis
15	Vascular endothelial growth factor receptor 2	KDR	3.527	0.003	Angiogenesis

Table 1. Differentially expressed proteins associated with angiogenesis and fibrosis in the aqueous humor of patients with neovascular age-related macular degeneration (nAMD).

Discussion

A previous study revealed that apatinib exhibited a potent inhibitory action on VEGF-induced proliferation, migration, and cord formation in human retinal microvascular endothelial cells[9]. In mice with oxygen-induced retinopathy or laser-induced CNV, a single intravitreal injection of apatinib inhibited VEGFR2 phosphorylation and significantly suppressed ocular neovascularization without retinal toxicity[9]. According to previous studies, VEGF/VEGFR2 signaling activation is involved in not only angiogenesis but also fibrosis through pathway-mediated cross-talk[22–24].

Despite being a pilot study, our aqueous humor proteomics analysis of nAMD patients showed that seven proteins (ANPEP, APOA4, CCN3, ERAP1, FLT1, KDR, and PPBP) involved in angiogenesis, as well as seven proteins (CAT, CFD, COL1A1, FLT1, LGALS1, SERPINA1, and TIMP1) involved in fibrosis, were all upregulated. Moreover, quantitation of VEGFR1 (FLT1) and VEFGR2 (KDR), which induce angiogenesis and fibrosis, revealed that their expression in the aqueous humor was significantly higher in nAMD than in control. This suggests that VEGFR2 inhibition could potentially serve as an alternative therapeutic option for nAMD. Therefore, inhibition of the VEGF signaling pathway using VEGFR2 tyrosine kinase inhibitors has emerged as a promising therapeutic strategy to reduce excessive neovascularization and fibrosis in chorioretinal diseases.

The current study evaluated the effects of apatinib on VEGFA and αSMA expression in nAMD models. Notably, our results showed that apatinib significantly reduced VEGFA release in TCM-treated ARPE-19 cells. According to previous reports, activated macrophages are associated with the pathological process of AMD[25,26]. In addition, Shaik-Dasthagirisaheb et al. have shown that VEGF mediates angiogenesis and inflammation[27]. Thus, apatinib could inhibit VEGF production and cellular response through activated macrophages. This can be regarded as evidence that apatinib may suppress the production of VEGF by regulating macrophage-induced pro-inflammatory mediators. Apatinib co-treatment also decreased TCM-induced αSMA expression in ARPE-19 cells. Previous studies have suggested that αSMA expression increases fibroblast contractile activity and plays an important role in local adhesion maturation[28,29]. In another previous study, several stromal cells were immunoreactive to αSMA in surgically removed CNV from nAMD patients[30]. These findings suggest that apatinib may inhibit CNV and subretinal fibrosis by reducing VEGF and αSMA expression. As such, our results encourage the further examination on the protective effects of apatinib in animal models of nAMD. The current study also confirmed that apatinib treatment significantly reduced VEGFA and αSMA in mice with laser-induced CNV. After studying effects of apatinib in mice with laser-induced CNV based on administration routes, we showed that both subconjunctival administration and intravitreal injection of apatinib significantly reduced VEGFA and αSMA expression and laser-induced CNV area. On OCT, hyper-reflective lesions appear as a complex of fluid, fibrin, blood, and CNV that exists under the retina, typically observed in nAMD patients[21]. Although these lesions were remarkably increased in mice with laser-induced CNV, apatinib co-administration was able to effectively reduce the size of the hyper-reflective lesions. This OCT finding is quite significant as it shows that anti-neovascularization and anti-fibrosis effects were achieved in the retina of a living animal model of nAMD.

Other previous studies have shown that VEGFA potently induced STAT3 activities. When comparing the time course of STAT3 activation to that of VEGFR2, the peak of STAT3 phosphorylation lagged behind VEGFR2, suggesting that STAT3 may act downstream of VEGFR2 to promote the proliferative events induced by VEGFA[31,32]. In a liver fibrosis model, the co-expression of αSMA and p-STAT3 is evident in fibrotic lesions, as shown in the double staining results[15]. We were able to confirm that αSMA was also highly expressed in the fibrotic lesion areas of mice with laser-induced CNV. Furthermore, the current study was able to confirm that apatinib inhibits p-STAT3 expression in TCM-induced ARPE-19 cells, which serves as an in vitro model

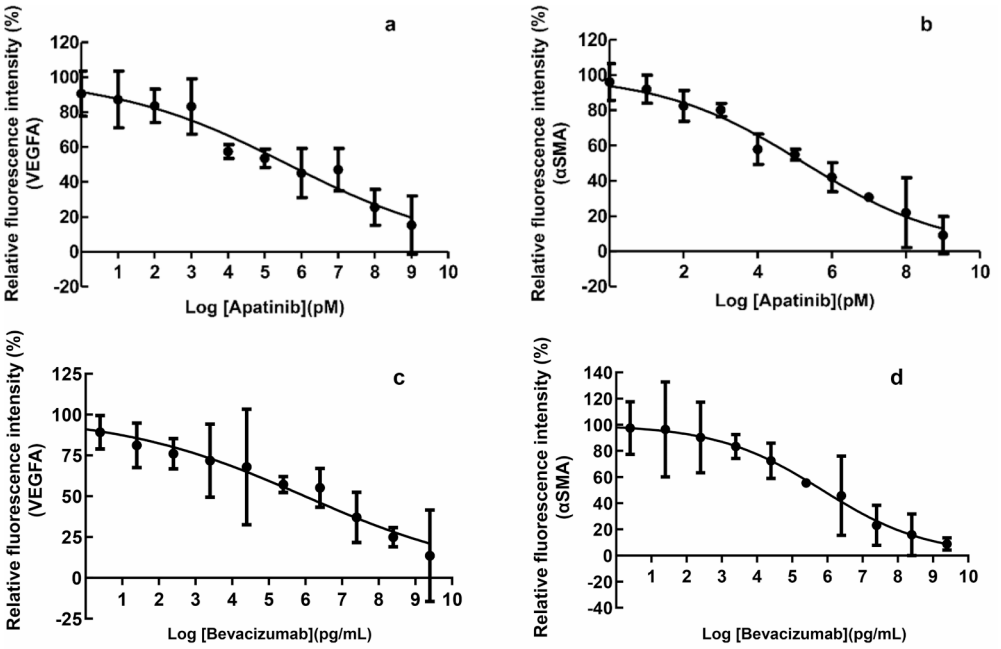

	IC_{50} of VEGFA	IC_{50} of α-SMA
Apatinib	215.9 ng/mL	91.1 ng/mL
Bevacizumab	969.6 ng/mL	716.6 ng/mL

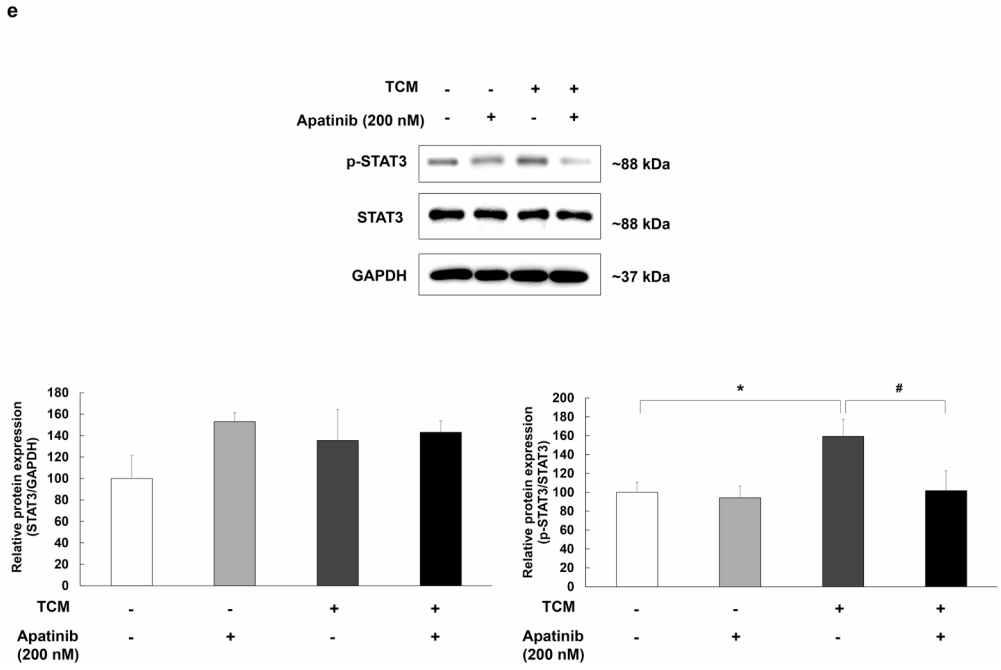

Fig. 3. The half maximal inhibitory concentration (IC_{50}) values of apatinib against VEGFA (**a**) and αSMA (**b**), bevacizumab against VEGFA (**c**) and αSMA (**d**). For afatinib, the IC_{50} values were 215.9 ng/mL for VEGFA and 91.1 ng/mL for αSMA. For bevacizumab, the IC_{50} values were 969.6 ng/mL for VEGFA and 716.6 ng/mL for αSMA. The data were fitted to log (concentration) and normalized response equations. The results are expressed as mean ± S.E. (n = 3). Suppressive effects of apatinib on THP-1-conditioned media (TCM)-induced STAT3 phosphorylation in ARPE-19 cells (**e**). Western blot analysis was used to examine the expression of p-STAT3 in ARPE-19 cells. ARPE-19 cells were stimulated by TCM for 3 h in 6-well plates and then treated with apatinib (200 nM) for 24 h. Thereafter, the whole lysate was analyzed for protein expression. Data were analyzed using two-way ANOVA (*$p < 0.05$ vs. untreated group, $^{\#}p < 0.05$ vs. only TCM (+) group), and the results are expressed as mean ± S.E. (n = 3). Uncropped blot images are presented in supplementary information (Supplementary Fig. S3).

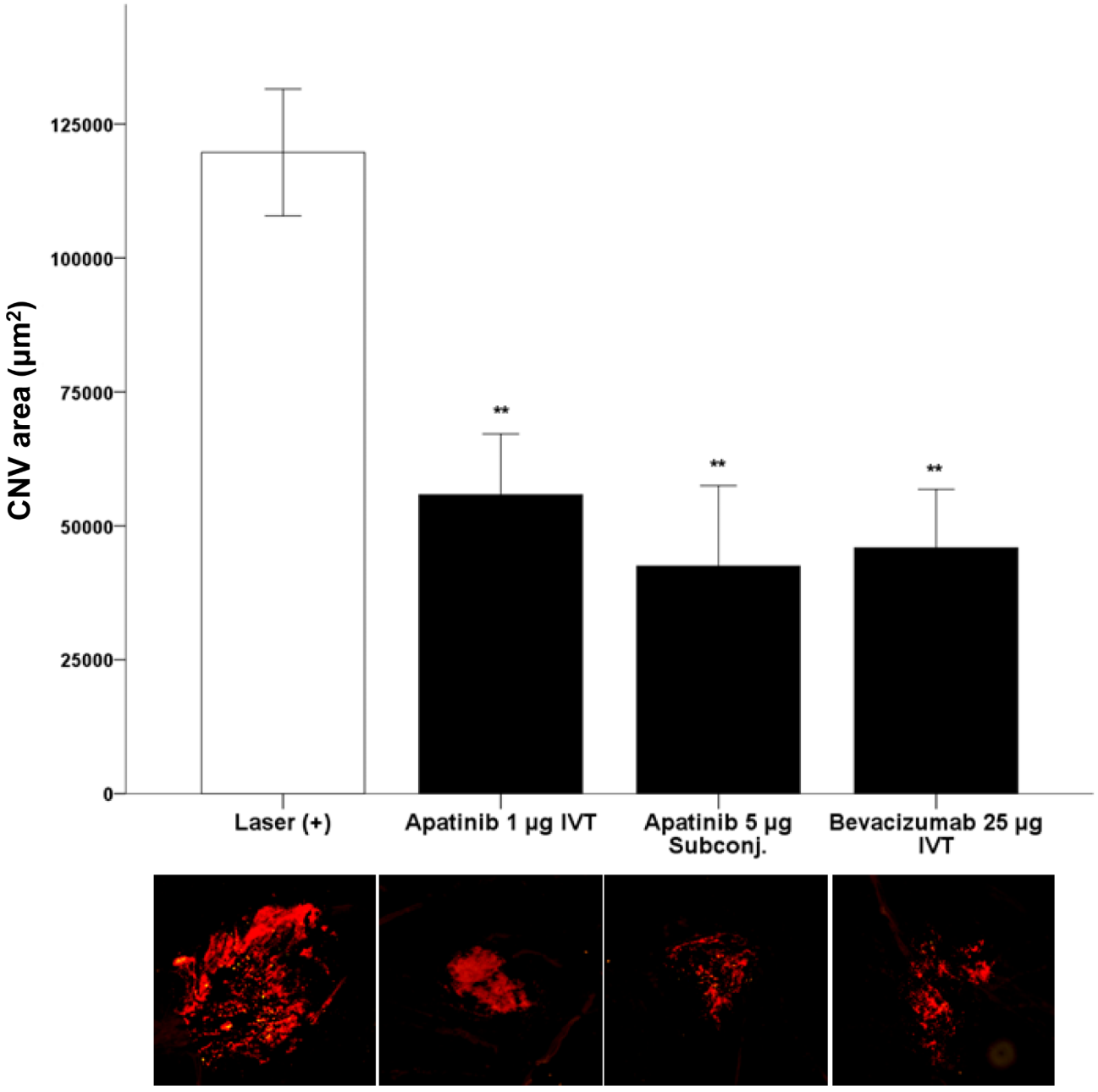

Fig. 4. Change in the laser-induced choroidal neovascularization (CNV) area after intravitreal treatment (IVT) or subconjunctival treatment (subconj.) with apatinib and bevacizumab in mice with laser-induced CNV. Laser setting (300 mW, 100 ms, 95% white bubble, 78 D lens). CNV was stained using Alexa Fluor 594-conjugated isolectin B4 (1:100 dilution). Data were analyzed using the Mann–Whitney U test (**$p < 0.01$ vs. only laser-induced CNV) and are expressed as the mean ± S.E. (n = 6–17).

of nAMD. This demonstrates that apatinib-induced VEGFR2 inhibition also exerts anti-angiogenic and anti-fibrotic effects by suppressing STAT3 activation in both in vitro and in vivo models of nAMD.

The current study has several limitations worth noting, including the relatively small sample size. Although these in vitro and in vivo models can adequately express the pathophysiology of nAMD, they cannot completely replace the pathophysiological processes that occur in real patients with nAMD.

In conclusion, our findings showed that apatinib, a selective VEGFR2 inhibitor, could reduce not only CNV but also subretinal fibrosis via αSMA by inhibiting the VEGF/VEGFR2 signaling pathway in a nAMD model. Therefore, VEGFR2 signaling pathway appears to play a pivotal role in the development of nAMD by regulating angiogenesis and fibrosis.

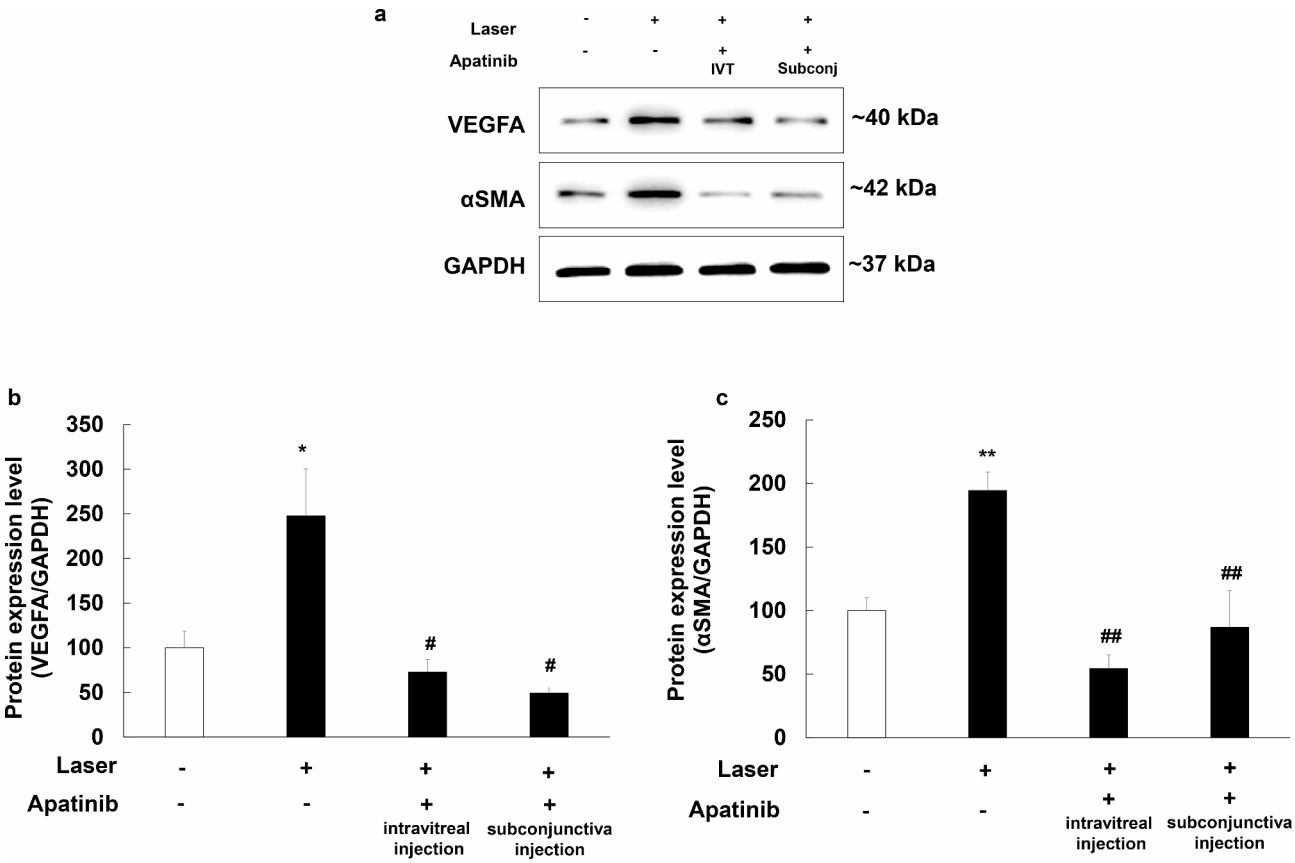

Fig. 5. Inhibitory effects of apatinib on VEGFA (**b**) and αSMA (**c**) expression in the mouse model of laser-induced choroidal neovascularization (CNV). Intravitreal (IVT) injection of apatinib (1 μg in 1 μL DMSO) and subconjunctival (subconj) injection of apatinib (5 μg in 1 μL DMSO) were administered immediately after laser photocoagulation. Equal amounts of protein from eye tissue lysates of mice with laser-induced CNV were analyzed for the expression of the indicated proteins. Protein expression in the eyes of mice with laser-induced CNV was measured 1 week after laser photocoagulation by Western blot analysis (**a**). Data were analyzed using one-way ANOVA (*$p < 0.05$ and **$p < 0.01$ vs. non-laser exposed group, $^{\#}p < 0.05$ and $^{\#\#}p < 0.01$ vs. only laser exposed group). The results are expressed as mean ± S.E. (n = 5–12). Uncropped blot images are presented in supplementary information (Supplementary Fig. S4).

Materials and methods

Ethics statement

All procedures and animal care were performed in accordance with the ARVO Statement for the Use of Animals in Ophthalmic and Vision Research and the ARRIVE guidelines. Approval for the study protocols was obtained from the Chungbuk National University Institutional Animal Care and Use Committee (CBNU IACUC) and complied with the Korean National Institute of Health Guide for the Care and Use of Laboratory Animals (CBNUA-2029-22-01).

Additionally, our study protocol was reviewed and approved by the Institutional Human Experimentation Committee Review Board of Ulsan University Hospital, Ulsan, Republic of Korea (NON2020-004 and UUH2018-03-006). This study was also conducted based on the ethical standards outlined in the 1964 Declaration of Helsinki. Informed consent was obtained from all patients for being included in the study.

Aqueous humor sampling

A total of 28 participants were enrolled in this study, with 14 patients in the nAMD group and 14 controls without nAMD. The control group consisted of patients without nAMD randomly selected from those undergoing macular hole surgery. The selection was based on their ages being similar to those in the nAMD group (Supplementary table S1). All nAMD patients received anti-VEGF intravitreal injections. Aqueous humor samples were collected at the beginning of the macular hole surgery or first intravitreal injection procedure. The process involved sterile surgical draping, placement of a sterile eyelid speculum, instillation of 1–2 drops of 0.5% proparacaine hydrochloride (alcaine, Alcon, Ft. Worth, TX, USA), and 5% povidone iodine immediately before surgery or injection. Anterior chamber paracentesis was conducted using a 30-gauge needle mounted on a 1 mL syringe, through a puncture at the peripheral cornea under a surgical microscope. Aqueous humor sample volumes ranged from 50 to 100 μL. Subsequently, the samples were transferred to microtubes and immediately stored at −70 °C. Our study protocol received approval from the Institutional Human Experimentation

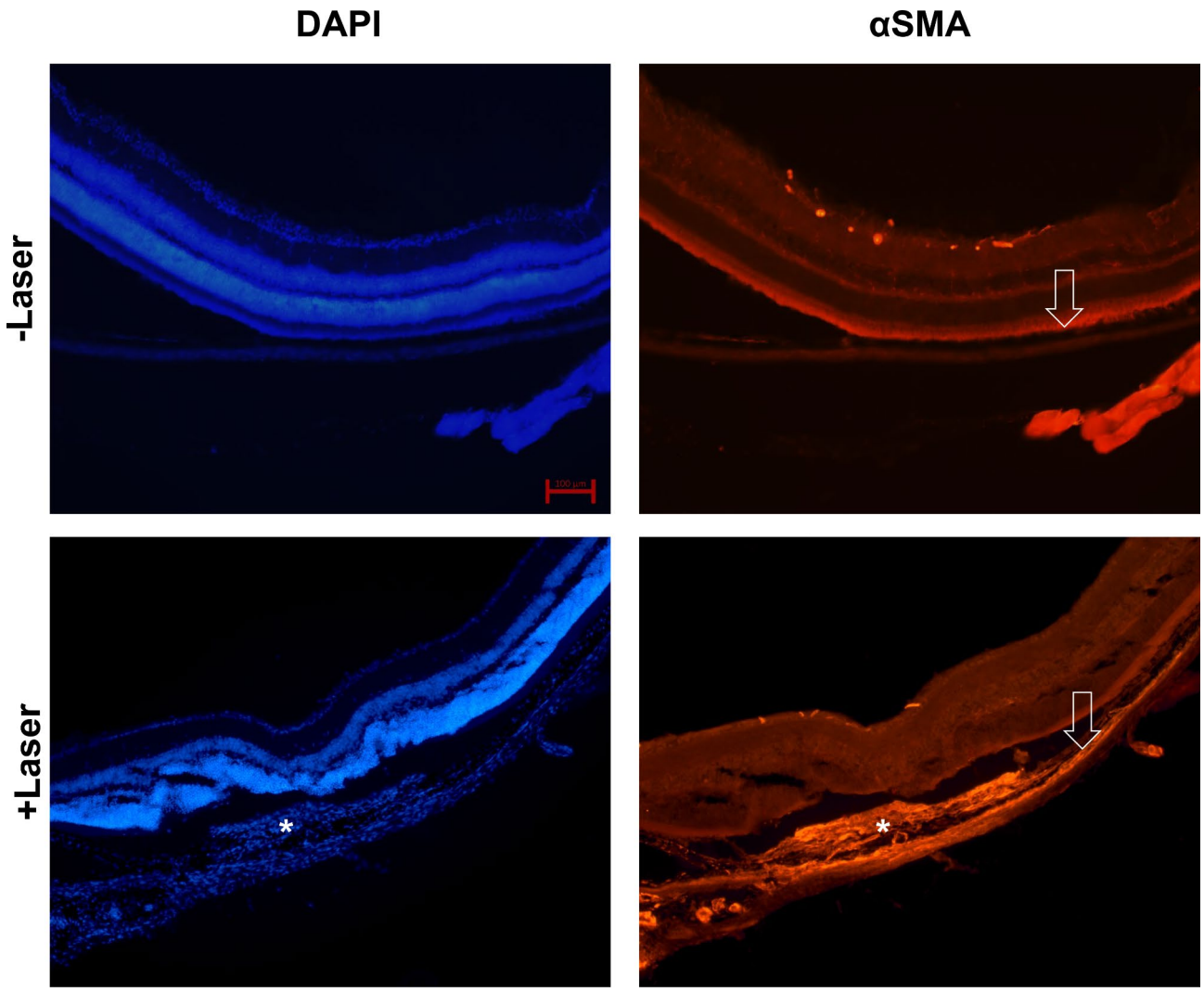

Fig. 6. Expression of αSMA in the eyes of mice with laser-induced choroidal neovascularization (CNV). Immunohistochemical staining of the eyes of mice with and without laser-induced CNV (DAPI, blue color and αSMA, orange color). White asterisks indicate subretinal fibrosis and deposits and increased αSMA expression level. The white arrow depicts the retinal pigment epithelium layer. Scale bar for each image: 100 μm.

Committee Review Board of Ulsan University Hospital, Ulsan, Republic of Korea (Approval Nos. NON2020-004 and UUH2018-03-006). The study adhered to the ethical principles outlined in the 1964 Declaration of Helsinki, and informed consent was obtained from all participating patients.

Protein digestion and tandem mass tag (TMT) labeling for liquid chromatography with tandem mass spectrometry (LC-MS/MS) analysis

To investigate the proteome of the aqueous humor, the collected samples (14 nAMD and 14 control) were combined and digested. The protein concentration of each sample was determined using the Bicinchoninic Acid (BCA) Protein Assay from Pierce. Each sample with 80 μg of protein was reduced with 10 mM dithiothreitol (DTT) for 30 min at 56 °C. Next, alkylation was carried out with 20 mM iodoacetamide, incubating the samples for 30 min in the dark at room temperature. Trypsin-LysC was added in a 50:1 protein-to-enzyme ratio, and the samples were enzymatically digested overnight at 37 °C. Desalting was done using an Oasis HLB cartridge. The enzymatic digests were resuspended in 0.1 M TEAB and labeled with two different TMTs following the manufacturer's protocol. The labeled samples were then pooled into one tube and dried under vacuum for further analysis.

Protein identification via LC-MS/MS analysis

To identify and quantify the aqueous humor proteome, we employed Q-Exactive Plus mass spectrometry paired with an Easy-nLC 1200 (Thermo Fisher Scientific, San Jose, CA, USA). The extracted peptides were dissolved in 0.1% formic acid and separated on an EASY-Spray column (C18, 2 μm particle size, 75 μm × 500 mm). The samples were eluted using a linear gradient of solvent B (80% acetonitrile, 0.1% formic acid; 5-50% over 120 min,

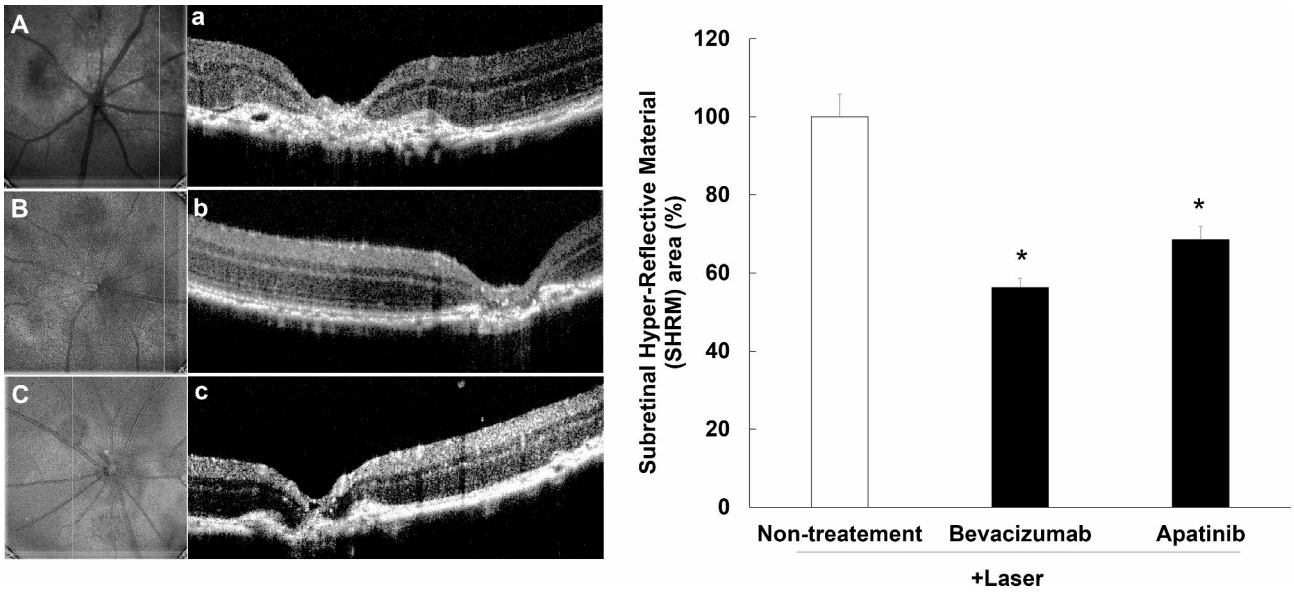

Fig. 7. Inhibitory effects of apatinib on the expression of hyper-reflective lesions in mice with laser-induced choroidal neovascularization (CNV). Laser photocoagulation spots were identified in digital red-free retinal images (non-treatment: (**A**) bevacizumab: (**B**) apatinib: (**C**). Using the center of the laser spot as reference, retinal OCT scans were performed in the vertical plane (non-treatment: (**a**) bevacizumab: (**b**) apatinib: (**c**). Hyper-reflective lesions were confirmed on OCT images. Thereafter, the inner border of the lesion was manually outlined, whereas the hyper-reflective area (mean area of vertical and horizontal planes) was measured using Image J software (version 1.53, https://imagej.nih.gov/ij/index.html). The hyper-reflective lesion area was significantly decreased after intravitreal administration of apatinib (1 μg/1 μL in DMSO) and bevacizumab as positive control (25 μg/1 μL) (**D**). Data were analyzed using the Kruskal–Wallis test followed by Dunn's test (*$p < 0.05$ vs. only laser-induced CNV group), and the results are expressed as mean ± S.E. ($n = 10–29$).

then 50-95% over 10 min at a flow rate of 300 nL/min). The ions were introduced to the mass spectrometer at 2.1 kV via electrospray. MS/MS spectra were obtained in data-dependent mode, focusing on the 20 most abundant peaks from the full MS scan with a fragmentation normalized collision energy of 32%. The dynamic exclusion time was set to 30 s, and the isolation window was 1.2 m/z. MS spectra were collected across a range of 350–2000 m/z, with a resolution of 70,000 at m/z 200. MS/MS spectra had a resolution of 17,500.

Database searches and TMT quantitation

Proteome Discoverer (Thermo Fisher Scientific, version 2.2.0.388) and Scaffold (version 4.10.0, Proteome Software Inc.) were used for database searches. SEQUEST and X!Tandem were configured to search the uniprot-proteome_HomoSapiens_82492_FASTA database, with a fragment ion mass tolerance of 0.02 Da and a parent ion tolerance of 10.0 PPM. SEQUEST and X!Tandem specified fixed modifications like cysteine carbamidomethylation and TMT6 plex of lysine. X!Tandem also included variable modifications such as Glu to pyro-Glu, ammonia loss, Gln to pyro-Glu at the N-terminus, oxidation of methionine, and N-terminal acetylation. SEQUEST listed oxidation of methionine and N-terminal acetylation as variable modifications. Protein identifications were accepted if they had a probability exceeding 5.0%, an FDR below 5.0%, and at least one identified peptide.

Scaffold Q+ (version 4.10.0) was used for TMT-based quantitation of peptides and proteins. Peptide identifications were accepted with a probability above 95.0% using the Scaffold Local FDR algorithm. Protein identifications were accepted if they had a probability exceeding 5.0%, an FDR below 5.0%, and at least two identified peptides. Protein intensities from each TMT experiment were log2-transformed and normalized by median. Statistical analysis to identify significant protein differences between nAMD and control groups across three TMT experiments involved a two-sided Student's t-test with a permutation-based FDR threshold (250 randomizations, FDR 0.05). Proteins were considered differentially regulated if their adjusted p-value yielded an FDR below or equal to 0.05, and their log2 fold-change ratio was ≤ -1.5 or $\geq +1.5$.

Gene ontology (GO) and functional analysis

The GO terms in the protein datasets were analyzed using the Scaffold bioinformatics resource (version 4.10.0) and DAVID (https://david.ncifcrf.gov/tools.jsp), which performs functional classification and ID conversion of the proteins identified. The "biological process," "molecular function," and "cellular component" classifications were analyzed using UniProt accession numbers.

Cell culture

In accordance with previous studies[33], ARPE-19 cells (a human RPE cell line from ATCC, Manassas, VA, USA) were cultured in DMEM supplemented with 10% FBS and antibiotic–antimycotic at 37 °C with 5% CO_2. Media were changed three times weekly. For subculture, cells were treated with 0.5% trypsin-EDTA, followed by resuspension in complete DMEM and seeding into 96-well plates at a density of 1×10^4 cells/well.

In vitro nAMD model (THP-1-conditioned medium model)

THP-1 cells activated by lipopolysaccharide (LPS) have been widely employed as a model to study inflammation[34]. Based on previous research[33], THP-1-conditioned media (TCM) was obtained following the described experimental procedure. Briefly, THP-1 cells, derived from human monocytes (Korean Cell Line Bank, Seoul, Korea, KCLB-40202), were cultured in RPMI-1640 medium supplemented with 10% FBS, 1% 2-mercaptoethanol, and antibiotic–antimycotic at 37 °C with 5% CO2. Upon confluence, cells were seeded in 12-well plates and differentiated with 200 ng/mL PMA overnight. Following PMA treatment, cells were stimulated with 1 μg/mL LPS in RPMI-1640. After 24 h, TCM were collected by centrifugation to remove cells and debris.

VEGFA and αSMA analysis in anin vitro nAMD model

ARPE-19 cells were plated in 96-well plates at a density of 10,000 cells per well. On the following day, the cells were treated with either 0.1% DMSO in RPMI1640 complete media or various concentrations of apatinib in a dose-dependent manner (ranging from 1 mM to 1 pM, including 100 μM, 10 μM, 1 μM, 100 nM, 10 nM, 1 nM, 100 pM, 10 pM, and 0 nM). The treatment was conducted in TCM for 3 h. The cells were then washed with phosphate buffer solution (PBS; Life Technologies, Carlsbad, CA, USA) and fixed in 4% paraformaldehyde (PFA) for 20 min at room temperature. Subsequently, the cells were permeabilized with 0.2% Triton X-100 in PBS for 15 min. After blocking with PBS containing with 5% bovine serum albumin (BSA; GenDEPOT, TX, USA, A0100) for 1 h, the cells were subsequently incubated overnight at 4 °C with VEGFA (Santa Cruz Biotechnology, CA, USA, SC-7269, 1:300) or αSMA (Abcam, Cambridge, UK, ab5694, 1:300) in blocking buffer. Thereafter, the cells were incubated with the appropriate Alexa Fluor 568-conjugated goat anti-rabbit IgG (Abcam, ab175471, 1:500) or Alexa Fluor 488-conjugated goat anti-mouse IgG (Abcam, ab150113, 1:500) diluted in 5% BSA for 2 h at room temperature. Subsequently, the cells were stained with 4′,6-diamidino-2-phenylindole (DAPI) for 5 min at room temperature in the absence of light, followed by quantification of fluorescence intensity using a FlexStation 3 Multi-Mode Microplate Reader (Molecular Devices, LLC, Sunnyvale, CA, USA).

In vivo CNV model and drug treatment

As described previously[33], 8-week-old male C57BL/6 N mice (Dae-Han Biolink, Korea) were used for the study. They were housed in standard cages with 4–5 mice per cage. Before the procedure, the mice were anesthetized with an intraperitoneal injection of 1.2% avertin and their pupils were dilated using 0.5% tropicamide and phenylephrine (Mydrin-P; Santen, Osaka, Japan). Laser photocoagulation was performed around the retina using a laser indirect ophthalmoscope. Immediately after the laser photocoagulation procedure,, a small amount of vitreous fluid was removed with a 30-gauge needle. Thereafter, mice were intravitreally injected with 1 μL of DMSO or apatinib (1 μg in 1 μL of DMSO) or bevacizumab (25 μg/1 μL; Genentech, San Francisco, CA, USA) at the same puncture site using a 32-gauge needle attached to a 5-μL Hamilton micro syringe (Hamilton, Reno, NV, USA). Apatinib (5 μg in 1 μL of DMSO) was also subconjunctivally administered in mice. A week later, all mice were euthanized through quick cervical dislocation.

Western blot

Western blotting was performed as described previously[33]. Mouse retina, RPE, and choroid were sonicated in lysis buffer and centrifuged to extract total protein. ARPE-19 cells and aqueous humor samples from retinal disease patients underwent similar processing. Proteins were separated by electrophoresis on a 12% SDS-PAGE gel and transferred to PVDF membranes. They were then incubated overnight with specific antibodies (αSMA (Abcam, ab5694, 1:1000), VEGFA (Abcam, ab46154, 1:1000), STAT3 (124H6, Cell Signaling Technology), phospho-STAT3 (sc-8059, Santa Cruz), and GAPDH (2118 S, Cell Signaling Technology, 1:5,000)) and subsequently with HRP-conjugated secondary antibodies. The proteins were visualized using ECL substrate and detected with the FUSION Solo S system. Protein quantification was performed using Image J software.

Isolectin B4 staining of CNV lesions

In order to detect the vessels, isolectin B4 staining was performed as described previously[33,35]. Seven days after laser photocoagulation, mice were euthanized via cervical dislocation. The eyes were dissected, removing unnecessary tissues and separating the RPE, choroid, and sclera. These tissues were fixed with 4% PFA and permeabilized in 0.1% Triton X-100 before staining the CNV lesions with Alexa Fluor 594-conjugated isolectin B4. After washing with PBS, eye cups were flat-mounted onto slides with the sclera facing down using DPX mounting medium (Sigma-Aldrich). Fluorescent pictures were taken with a Zeiss Axio Imager A2 microscope.

Immunohistochemical staining

Immunohistochemical was performed as described previously[33]. After 7 days post laser photocoagulation, mice were euthanized and their eyes fixed overnight in 4% PFA at 4 °C. The eyes were then sliced into 15-μm thick sections using a Leica CM1850 microtome and underwent permeabilization in PBS with 0.3% Triton X-100 and 0.3% hydrogen peroxide. Subsequently, the sections were blocked with 5% BSA (including 1% goat serum) at room temperature for 1 h. Primary antibodies targeting αSMA (Abcam, ab5694, diluted 1:200 in 5% BSA) were applied and left overnight at 4 °C. Following PBS washing, the sections were treated with Alexa Fluor 568-conjugated goat anti-rabbit IgG (H + L) secondary antibody (Abcam, ab175471, diluted 1:500 in 5% BSA)

for 2 h at room temperature. Later, the sections were stained with DAPI (300 nM in 5% BSA; Sigma-Aldrich) for 20 min. Finally, the sections were mounted onto glass slides using mounting medium from Vector Laboratories, Inc., San Francisco, CA, USA, and images were taken using the ZEISS Axio Observer fluorescence microscope system.

Hyper-reflective lesion measurement using optical coherence tomography (OCT)

For all procedures, mice were anesthetized via intraperitoneal injection with 1.2% avertin (25 mL/kg). The pupils were dilated using a combination of 0.5% tropicamide and phenylephrine (Mydrin-P). Laser photocoagulation spots were detected in digital red-free retinal images utilizing Spectral Domain OCT (Eyemera OCT, IISCIENCE, San Jose, CA, USA). Retinal OCT scans were conducted twice in the vertical and horizontal planes, with the center of the laser spot serving as a reference point. Hyper-reflective lesions were confirmed on OCT images obtained from both planes. Subsequently, the inner border of the lesion was manually delineated, and the cross-sectional area of the hyper-reflective lesion was measured using Image J software.

Data analysis

The data underwent analysis using the Mann–Whitney U test in IBM SPSS Statistics version 21.0 for Windows (IBM Corp, Armonk, NY, USA). Additionally, One-way analysis of variance (ANOVA) was performed, followed by the Holm–Sidak method, using SigmaPlot 14 software (SYSTAT Software, San Jose, CA, USA). Prism software (GraphPad Software, Boston, MA, USA) was utilized to determine the half maximal inhibitory concentration (IC_{50}) and coefficient of determination (R2). Results are reported as means ± standard errors (S.E.).

Data availability

The datasets used and/or analysed during the current study are available from the corresponding authors on reasonable request.

Received: 3 May 2024; Accepted: 11 October 2024
Published online: 27 October 2024

References

1. Lambert, N. G. et al. Risk factors and biomarkers of age-related macular degeneration. *Prog. Retin. Eye Res.* **54**, 64–102. https://doi.org/10.1016/j.preteyeres.2016.04.003 (2016).
2. Witmer, A. N., Vrensen, G. F., Van Noorden, C. J. & Schlingemann, R. O. Vascular endothelial growth factors and angiogenesis in eye disease. *Prog. Retin. Eye Res.* **22**, 1–29. https://doi.org/10.1016/s1350-9462(02)00043-5 (2003).
3. Heier, J. S. et al. Ranibizumab for treatment of neovascular age-related macular degeneration: A phase I/II multicenter, controlled, multidose study. *Ophthalmology* **113**(633), e631-634. https://doi.org/10.1016/j.ophtha.2005.10.052 (2006).
4. Rosenfeld, P. J. et al. Ranibizumab for neovascular age-related macular degeneration. *N. Engl. J. Med.* **355**, 1419–1431. https://doi.org/10.1056/NEJMoa054481 (2006).
5. Heier, J. S. et al. Intravitreal aflibercept (VEGF trap-eye) in wet age-related macular degeneration. *Ophthalmology* **119**, 2537–2548. https://doi.org/10.1016/j.ophtha.2012.09.006 (2012).
6. Ho, A. C. et al. Twenty-four-month efficacy and safety of 0.5 mg or 2.0 mg ranibizumab in patients with subfoveal neovascular age-related macular degeneration. *Ophthalmology* **121**, 2181–2192. https://doi.org/10.1016/j.ophtha.2014.05.009 (2014).
7. Daniel, E. et al. Risk of scar in the comparison of age-related macular degeneration treatments trials. *Ophthalmology* **121**, 656–666. https://doi.org/10.1016/j.ophtha.2013.10.019 (2014).
8. Koch, S. & Claesson-Welsh, L. Signal transduction by vascular endothelial growth factor receptors. *Cold Spring Harb. Perspect. Med.* **2**, a006502. https://doi.org/10.1101/cshperspect.a006502 (2012).
9. Kim, K. L. & Suh, W. Apatinib, an inhibitor of vascular endothelial growth factor receptor 2, suppresses pathologic ocular neovascularization in mice. *Investig. Ophthalmol. Vis. Sci.* **58**, 3592–3599. https://doi.org/10.1167/iovs.17-21416 (2017).
10. Shibuya, M. Vascular endothelial growth factor (VEGF) and its receptor (VEGFR) signaling in angiogenesis: A crucial target for anti- and pro-angiogenic therapies. *Genes Cancer* **2**, 1097–1105. https://doi.org/10.1177/1947601911423031 (2011).
11. Luo, J. et al. Vascular endothelial growth factor promotes the activation of hepatic stellate cells in chronic schistosomiasis. *Immunol. Cell Biol.* **95**, 399–407. https://doi.org/10.1038/icb.2016.109 (2017).
12. Zhang, J. & Chu, M. Differential roles of VEGF: Relevance to tissue fibrosis. *J. Cell. Biochem.* **120**, 10945–10951. https://doi.org/10.1002/jcb.28489 (2019).
13. Alvarez, J. V. et al. Identification of a genetic signature of activated signal transducer and activator of transcription 3 in human tumors. *Cancer Res* **65**, 5054–5062. https://doi.org/10.1158/0008-5472.Can-04-4281 (2005).
14. Hwang, S. et al. Phosphorylation of STAT3 and ERBB2 mediates hypoxia-induced VEGF release in ARPE-19 cells. *Mol. Med. Rep.* **22**, 2733–2740. https://doi.org/10.3892/mmr.2020.11344 (2020).
15. Wang, Z., Li, J., Xiao, W., Long, J. & Zhang, H. The STAT3 inhibitor S3I–201 suppresses fibrogenesis and angiogenesis in liver fibrosis. *Lab. Investig.* **98**, 1600–1613. https://doi.org/10.1038/s41374-018-0127-3 (2018).
16. Tian, S. et al. YN968D1 is a novel and selective inhibitor of vascular endothelial growth factor receptor-2 tyrosine kinase with potent activity in vitro and in vivo. *Cancer Sci.* **102**, 1374–1380. https://doi.org/10.1111/j.1349-7006.2011.01939.x (2011).
17. Roviello, G. et al. Apatinib: A novel receptor tyrosine kinase inhibitor for the treatment of gastric cancer. *Cancer Lett.* **372**, 187–191. https://doi.org/10.1016/j.canlet.2016.01.014 (2016).
18. Chakraborty, D. et al. Activation of STAT3 integrates common profibrotic pathways to promote fibroblast activation and tissue fibrosis. *Nat. Commun.* **8**, 1130. https://doi.org/10.1038/s41467-017-01236-6 (2017).
19. Kasembeli, M. M., Bharadwaj, U., Robinson, P. & Tweardy, D. J. Contribution of STAT3 to inflammatory and fibrotic diseases and prospects for its targeting for treatment. *Int. J. Mol. Sci.* **19**, 2299. https://doi.org/10.3390/ijms19082299 (2018).
20. Xie, C. et al. Apatinib triggers autophagic and apoptotic cell death via VEGFR2/STAT3/PD-L1 and ROS/Nrf2/p62 signaling in lung cancer. *J. Exp. Clin. Cancer Res.* **40**, 266. https://doi.org/10.1186/s13046-021-02069-4 (2021).
21. Willoughby, A. S. et al. Subretinal hyperreflective material in the comparison of age-related macular degeneration treatments trials. *Ophthalmology* **122**, 1846-1853.e1845. https://doi.org/10.1016/j.ophtha.2015.05.042 (2015).
22. Ou, X. M. et al. VEGFR-2 antagonist SU5416 attenuates bleomycin-induced pulmonary fibrosis in mice. *Int. Immunopharmacol.* **9**, 70–79. https://doi.org/10.1016/j.intimp.2008.10.002 (2009).
23. Yan, Z. et al. CD147 promotes liver fibrosis progression via VEGF-A/VEGFR2 signalling-mediated cross-talk between hepatocytes and sinusoidal endothelial cells. *Clin. Sci. (Lond.)* **129**, 699–710. https://doi.org/10.1042/cs20140823 (2015).

24. Su, X. et al. FN-EDA mediates angiogenesis of hepatic fibrosis via integrin-VEGFR2 in a CD63 synergetic manner. *Cell Death Discov.* **6**, 140. https://doi.org/10.1038/s41420-020-00378-9 (2020).
25. Oh, H. et al. The potential angiogenic role of macrophages in the formation of choroidal neovascular membranes. *Investig. Ophthalmol. Vis. Sci.* **40**, 1891–1898 (1999).
26. Cao, X. et al. Macrophage polarization in the maculae of age-related macular degeneration: A pilot study. *Pathol. Int.* **61**, 528–535. https://doi.org/10.1111/j.1440-1827.2011.02695.x (2011).
27. Shaik-Dasthagirisaheb, Y. B. et al. Vascular endothelial growth factor (VEGF), mast cells and inflammation. *Int. J Immunopathol. Pharmacol.* **26**, 327–335. https://doi.org/10.1177/039463201302600206 (2013).
28. Hinz, B., Celetta, G., Tomasek, J. J., Gabbiani, G. & Chaponnier, C. Alpha-smooth muscle actin expression upregulates fibroblast contractile activity. *Mol. Biol. Cell* **12**, 2730–2741. https://doi.org/10.1091/mbc.12.9.2730 (2001).
29. Hinz, B., Dugina, V., Ballestrem, C., Wehrle-Haller, B. & Chaponnier, C. Alpha-smooth muscle actin is crucial for focal adhesion maturation in myofibroblasts. *Mol. Biol. Cell* **14**, 2508–2519. https://doi.org/10.1091/mbc.e02-11-0729 (2003).
30. Ishikawa, K., Kannan, R. & Hinton, D. R. Molecular mechanisms of subretinal fibrosis in age-related macular degeneration. *Exp. Eye Res.* **142**, 19–25. https://doi.org/10.1016/j.exer.2015.03.009 (2016).
31. Liao, X. H. et al. STAT3 protein regulates vascular smooth muscle cell phenotypic switch by interaction with myocardin. *J. Biol. Chem.* **290**, 19641–19652. https://doi.org/10.1074/jbc.M114.630111 (2015).
32. Liao, X. H. et al. VEGF-A stimulates STAT3 activity via nitrosylation of myocardin to regulate the expression of vascular smooth muscle cell differentiation markers. *Sci. Rep.* **7**, 2660. https://doi.org/10.1038/s41598-017-02907-6 (2017).
33. Yu, E. et al. Alpinumisoflavone ameliorates choroidal neovascularisation and fibrosis in age-related macular degeneration in in vitro and in vivo models. *Sci. Rep.* **12**, 14316. https://doi.org/10.1038/s41598-022-18531-y (2022).
34. Chanput, W., Mes, J. J. & Wichers, H. J. THP-1 cell line: An in vitro cell model for immune modulation approach. *Int. Immunopharmacol.* **23**, 37–45. https://doi.org/10.1016/j.intimp.2014.08.002 (2014).
35. Léger, H., Santana, E., Beltran, W. A. & Luca, F. C. Preparation of mouse retinal cryo-sections for immunohistochemistry. *J. Vis. Exp.*https://doi.org/10.3791/59683 (2019).

Acknowledgements

This research was supported by "Regional Innovation Strategy (RIS)" through the National Research Foundation of Korea (NRF) funded by the Ministry of Education (MOE) (2021RIS-001), the National Research Foundation of Korea (NRF) grant funded by the Korea government (MSIT) (No. MRC, 2017R1A5A2015541), (No. NRF-2022R1F1A1069431) and the Ministry of Food and Drug Safety (20182MFDS425, 22214MFDS252, and 23212MFDS217). This research was also supported by Ulsan University Hospital Research Grant (UUH-2020-07).

Author contributions

Conceptualization, J.K.M., J.M.W. and J.Y.; methodology, E.Y, J.J., J.K.M. and J.Y.; investigation, E.Y., H.K., H.P., J.H.H., Y.S., J.K.M. and J.Y. ; data curation, J.K.M. and J.Y.; formal analysis, E.Y., H.K. and Y.S.; writing—original draft preparation, E.Y. and J.K.M; writing—review and editing, J.K.M. and J.Y.; visualization, E.Y. and H.K.; funding acquisition, J.K.M. and J.Y.; supervision, J.K.M. and J.Y.; project administration, J.K.M. and J.Y. All authors have read and agreed to the publication of the current version of the manuscript.

Declarations

Competing interests

The authors declare no competing interests.

Additional information

Supplementary Information The online version contains supplementary material available at https://doi.org/10.1038/s41598-024-76258-4.

Correspondence and requests for materials should be addressed to J.K.M. or J.Y.

Reprints and permissions information is available at www.nature.com/reprints.

Publisher's note Springer Nature remains neutral with regard to jurisdictional claims in published maps and institutional affiliations.

Open Access This article is licensed under a Creative Commons Attribution-NonCommercial-NoDerivatives 4.0 International License, which permits any non-commercial use, sharing, distribution and reproduction in any medium or format, as long as you give appropriate credit to the original author(s) and the source, provide a link to the Creative Commons licence, and indicate if you modified the licensed material. You do not have permission under this licence to share adapted material derived from this article or parts of it. The images or other third party material in this article are included in the article's Creative Commons licence, unless indicated otherwise in a credit line to the material. If material is not included in the article's Creative Commons licence and your intended use is not permitted by statutory regulation or exceeds the permitted use, you will need to obtain permission directly from the copyright holder. To view a copy of this licence, visit http://creativecommons.org/licenses/by-nc-nd/4.0/.

© The Author(s) 2024